PHYSICAL REVIEW A VOLUME 21, NUMBER 1 JANUARY 1980

Angular distributions of photoelectrons from resonant two-photon ionization of sodium through the $3p\ ^2P_{3/2}$ intermediate state

John C. Hansen, John A. Duncanson, Jr.,* Ring-Ling Chien, and R. Stephen Berry
Department of Chemistry and the James Franck Institute, The University of Chicago, Chicago, Illinois 60637
(Received 1 May 1979)

Angular distributions of photoelectrons from resonant two-photon ionization of sodium have been measured. Excitation and ionization were carried out with two pulsed lasers, one with a frequency resonant with the $3s\ ^2S_{1/2} \rightarrow 3p\ ^2P_{3/2}$ transition. The hyperfine levels in the intermediate state were excited coherently; hyperfine coupling affects the photoelectron distributions through a dependence on the time interval between excitation and ionization. The results are analyzed to give values of three microscopic parameters: the ratio of the radial dipole matrix elements for the production of $l = 0$ and $l = 2$ final states from the $3p$ level, the difference of the phase shifts of the outgoing electron in the final channels, and a parameter which expresses the depolarizing effect of the nuclear spin on the intermediate state. The phase-shift difference agrees with extrapolated bound-state data, but the final state has more s character than theoretical quantum-defect calculations suggest.

INTRODUCTION

This work is part of a continuing study of multiphoton ionization, particularly of the angular distributions of photoelectrons from these processes.[1-5] The angular distribution produced by ionization of an isotropic ensemble is restricted by the polarization states of the photons participating in the process.[6-9] Hence multiphonon ionization produces angular distributions containing more information than the distributions from single-photon ionization.[1,7,8] This information concerns the initial and intermediate states from which the photoelectron is ejected, the transition amplitudes to the individual waves of the free electron, the state of the remaining core, the effect of any interaction between the core and the free electron, and the nature of the radiation field causing the transition.[1,10-12] In principle, multiphoton ionization can be used as a sensitive probe to study the bound excited and continuum states of molecules. The eventual goal of this work is to use this method to study the excited states of molecules.

The experiment reported here, resonant two-photon ionization of sodium through the $3p\ ^2P_{3/2}$ level, in spite of its simplicity, contains some of the features we expect to see in more complex systems. The atoms are excited by a pulsed tunable dye laser set to the resonant excitation frequency of the $3s\ ^2S_{1/2} \rightarrow 3p\ ^2P_{3/2}$ transition and are then ionized by a pulse of ultraviolet radiation from a nitrogen laser. Two partial waves, $l=0$ and $l=2$, constitute the final state, so their branching ratio and the difference of their phase shifts influence the results. Also, because of the short durations of our laser pulses, the intermediate state is a superposition, at least partially coherent, of hyperfine states. Thus the angular distributions are affected by the hyperfine splittings, the laser pulse durations, and the time between excitation and ionization.[5,13-15] The distributions of photoelectrons from the $j=\frac{3}{2}$ intermediate state exhibit the most general phenomenological form allowed for ionized by two linearly polarized photons (in contrast to an intermediate state with $j=\frac{1}{2}$, where spherical symmetry causes some of the possible terms to be zero[4]). As a result, three microscopic parameters, the ratio of the $3p \rightarrow ks$ and $3p \rightarrow kd$ radial matrix elements, the difference of the s and d wave phase shifts, and a parameter associated with the degree of coherence of the hyperfine levels may be determined. The data are obtained from angular distributions of electrons produced with various angles between the polarized vectors of the two light beams. The time dependence of the coherent intermediate state reflects itself in the variation of the angular distributions measured with different time delays between the first and second light pulses.

In this report, we first review the theoretical results necessary for the interpretation of our data. A description of the experiment and the method of data analyses follows. Finally, we discuss the results of the experiment and compare them with theoretical predictions. The branching ratio is somewhat higher than predicted but the phase shifts are consistent with extrapolated quantum defects. The time-evolution parameter varies as expected with the time delay between laser pulses.

REVIEW OF THEORY

Resonant two-photon ionization may be regarded as a two-step process in which the first photon

creates an intermediate state corresponding to an ensemble which is not, in general, isotropic. For linearly polarized light in both photon beams, in the dipole approximation, the most general form of the angular distribution is[6]

$$I(\theta,\phi)=\alpha_{00}P_{00}(\cos\theta)+\alpha_{20}P_{20}(\cos\theta)+\alpha_{40}P_{40}(\cos\theta)$$
$$+\alpha_{21}P_{21}(\cos\theta)\cos\phi$$
$$+\alpha_{41}P_{41}(\cos\theta)\cos\phi$$
$$+\alpha_{22}P_{22}(\cos\theta)\cos2\phi+\alpha_{42}P_{42}(\cos\theta)\cos2\phi \qquad (1)$$

in the coordinate system shown in Fig. 1. The α_{LM}'s in general depend upon η, the angle between the two polarization vectors. A theoretical treatment of this problem with particular emphasis on electron polarization and circularly polarized light was recently given by Nienhuis, Granneman, and van der Wiel[14]; one could use their formalism to derive Eq. (1).

Suppose the electron in the intermediate state has a definite orbital angular momentum quantum number l. In the dipole approximation conventional optical selection rules apply and the available final channels for the free electron are those with orbital angular momenta $l+1$ and $l-1$. The angular distribution depends upon the ratio of the radial matrix elements for the second transition $\sigma_{l-1}/\sigma_{l+1}$ and the difference of the phase shifts of the two final states $(\delta_{l-1}-\delta_{l+1})$. In the absence of time-dependent effects in the intermediate state a straightforward theoretical analysis gives values of the coefficients α_{LM} as functions of these two atomic parameters and η. The forms of these functions depend upon the angular momentum coupling schemes appropriate for the description of the intermediate and final states.

In the experiment reported here the intermediate level $(3p\,^2P_{3/2})$ is a superposition of the hyperfine states shown in Fig. 2. The time evolution of this state, between excitation and ionization, must be considered. The analysis of this evolution assumes that the bandwidth of the light causing excitation is much greater that the separations of the relevant hyperfine states so that the spectral density of the radiation field is the same for all hyperfine transitions. We also assume, in correspondence with our experimental conditions, that the transition rates are linear in the light intensity for both pulses. In the general analysis no simplifying assumptions concerning the light-pulse durations were made because under our experimental conditions neither limiting case (instantaneous pulses or cw light) applies.[13,14] With light of a sufficiently broad bandwidth (or equivalently, a short coherence time) the excitation may be regarded as an instantaneous event in which the nuclear spin is not affected. Immediately following excitation the electronic density operator reflects an alignment due to the photon's polarization while the nuclear density operator remains isotropic. Between excitation and ionization the elements of the density matrix connecting different hyperfine states oscillate with angular frequencies $\omega_{f'f''}=(E_{f'}-E_{f''})/\hbar$, where $E_{f'}$ and $E_{f''}$ are the energies of hyperfine states with total angular momenta f' and f'', respectively. Following an interval while the precession of the intermediate state occurs, the atom is ionized by a process which, like the first excitation, does not affect the nuclear spin and may be regarded as instantaneous. Thus the excitation and ionization processes are most conveniently described in the fine structure (FS) coupling scheme in which the density operators for electronic and nuclear angular momenta (j and

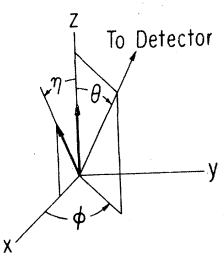

FIG. 1. Coordinate system used to describe the angular distributions. The polarization vector of the first photon lies in the xz plane; the polarization vector of the second photon coincides with the z axis.

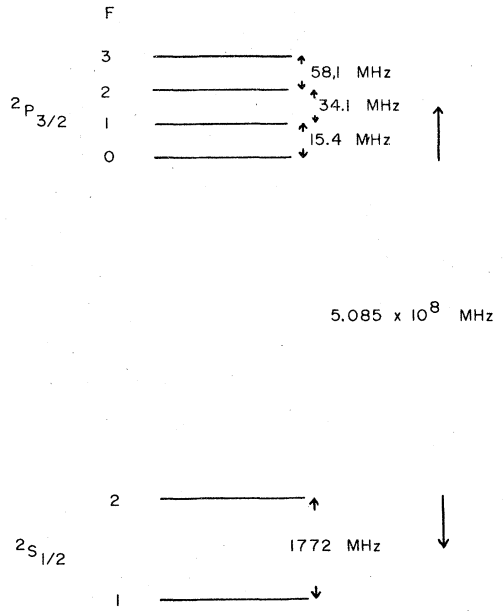

FIG. 2. Hyperfine levels of the $3s\,^2S_{1/2}$ and $3p\,^2P_{3/2}$ states of sodium.

i, respectively) are separately expanded in irreducible tensorial components $p_{JM}(jj)$ and $p_{I M_I}(ii)$. Because nuclear spin is not observed only its isotropic component $I=0$ need be considered. The hyperfine (hf) coupling scheme is appropriate for the description of the intermediate-state precession. In this basis the density operator is expanded in irreducible tensorial components $p_{JM}(f'f'')$, where f' and f'' are the angular momentum quantum numbers of two hyperfine states. Thus the time evolution of the $p_{JM}(jj)p_{00}(ii)$ component of the density operator is determined by performing a recoupling transformation to the hf basis, allowing the components $p_{JM}(f'f'')$ to precess, and transforming back to the FS basis, considering only the projection upon the $I=0$ subspace. So, as a function of time after excitation τ,

$$p_{JM}(jj)_{(\tau)} = p_{JM}(jj)_{(\tau=0)} W(J),$$

where

$$W(J) = \sum_{f'f''} (2J+1)(2f'+1)(2f''+1) \begin{Bmatrix} j & j & J \\ i & i & 0 \\ f' & f'' & J \end{Bmatrix}^2 \times e^{-i\omega_{f'f''}\tau} e^{-\Gamma\tau}.$$

The quantity in brackets is a 9-j symbol and radiative decay is included in the factor $e^{-\Gamma\tau}$. For an intermediate state excited by linearly polarized light only $J=0$ and $J=2$ components appear. The ratio $W(2)/W(0)$ is always less than unity and equals 1 only at $\tau=0$. The decrease in this ratio with increasing τ may be thought of as a transfer of electronic alignment to the nucleus as a result of the hyperfine coupling.

The functions $W(0)$ and $W(2)$ suffice to describe the effects of the hyperfine precession in an experiment in which the times of excitation and ionization are well defined. In our experiment, however, the durations of the light pulses are not negligible compared to the oscillation periods $2\pi/\omega_{f'f''}$. Hence the effects of time evolution are contained not in $W(J)$, but rather the functions $\chi(J)$, the convolutions of $W(J)$ with the intensity distributions of both light pulses, $I_1(t)$ and $I_2(t)$:

$$\chi(J) = \int_{-\infty}^{\infty} dt_2 \int_{-\infty}^{t_2} dt_1 W(J)(t_2 - t_1) I_1(t_1) I_2(t_2).$$

The $\chi(J)$'s are functions of the widths of the light pulses and the delay between them. The angular distributions are affected through their ratio $T_{20} = \chi(2)/\chi(0)$. Theoretical predictions of T_{20} have been made for Gaussian intensity distributions for the widths and time delays used in this experiment.[5] The most important result of this theoretical consideration of the hyperfine structure is the reduction of its effect on the angular distribution to the single parameter $\chi(2)/\chi(0)$.

The phenomenological coefficients α_{LM} are functions of four physical parameters, $\chi(2)/\chi(0)$, σ_0/σ_2, $\cos(\delta_0 - \delta_2)$, and η. In this experiment measurements are confined to the plane perpendicular to the propagation direction of the light ($\phi = 0, \pi$), so theoretical expressions are needed only for the angular distribution on this plane instead of the total angular distribution. When confined to this plane the general form is a linear combination of only five independent functions, not seven as in Eq. (1). If we choose these to be

$$\begin{aligned} I(\theta, \phi=0) &= C_{00} P_{00}(\cos\theta) + C_{20} P_{20}(\cos\theta) + C_{40} P_{40}(\cos\theta) \\ &\quad + C_{21} P_{21}(\cos\theta) + C_{41} P_{41}(\cos\theta), \end{aligned} \tag{2}$$

the coefficients C_{LM} can be expressed in terms of the microscopic parameters thus[5,15]:

$$\begin{aligned} C_{00} &= \tfrac{1}{9} A\{[2\chi(0) + (2 - 3\sin^2\eta)\chi(2)]\sigma_0^2 \\ &\quad + [4\chi(0) + (\tfrac{6}{5}\sin^2\eta + \tfrac{2}{5})\chi(2)]\sigma_2^2\}, \\ C_{20} &= A\tfrac{2}{9}\sqrt{\tfrac{1}{5}}\{-2[\chi(0) + (2 - 3\sin^2\eta)\chi(2)] \\ &\quad \times \sigma_0\sigma_2\cos(\delta_0 - \delta_2) \\ &\quad + [2\chi(0) + (\tfrac{5}{7} - \tfrac{3}{7}\sin^2\eta)\chi(2)]\sigma_2^2\}, \\ C_{40} &= A\tfrac{8}{35}(1 - 2\sin^2\eta)\chi(2)\sigma_2^2, \\ C_{21} &= A\sqrt{\tfrac{2}{15}}[-\sigma_0\sigma_2\cos(\delta_0 - \delta_2) + \tfrac{2}{7}\sigma_2^2]\chi(2)\sin 2\eta, \\ C_{41} &= A\tfrac{4}{7}\sqrt{\tfrac{1}{5}}\sigma_2^2\chi(2)\sin 2\eta. \end{aligned} \tag{3}$$

Here A is a constant which includes the transition amplitude for the $3s \rightarrow 3p$ transition. Its value does not affect our results because we determine only the relative magnitudes of the coefficients C_{LM}, not the values themselves.

Using measurements at several values of η (but the interval between pulses fixed) we made least-squares fits to Eq. (2). Then from the theoretical expressions (3) the atomic parameters σ_0/σ_2 and $\cos(\delta_0 - \delta_2)$ are determined. Also, by changing the delay between laser pulses, we observe changes in the angular distributions due to the hyperfine coupling. This allows us to calculate $\chi(2)/\chi(0)$ for different time delays. The methods used to find the best-fit values of these parameters are described below.

EXPERIMENTAL

A schematic diagram of the apparatus is shown in Fig. 3. The light from a nitrogen laser (N_2L), triggered at 60 Hz from line voltage, is divided into two beams, one of which pumps a tunable dye laser (DL). The wavelength of the dye laser is

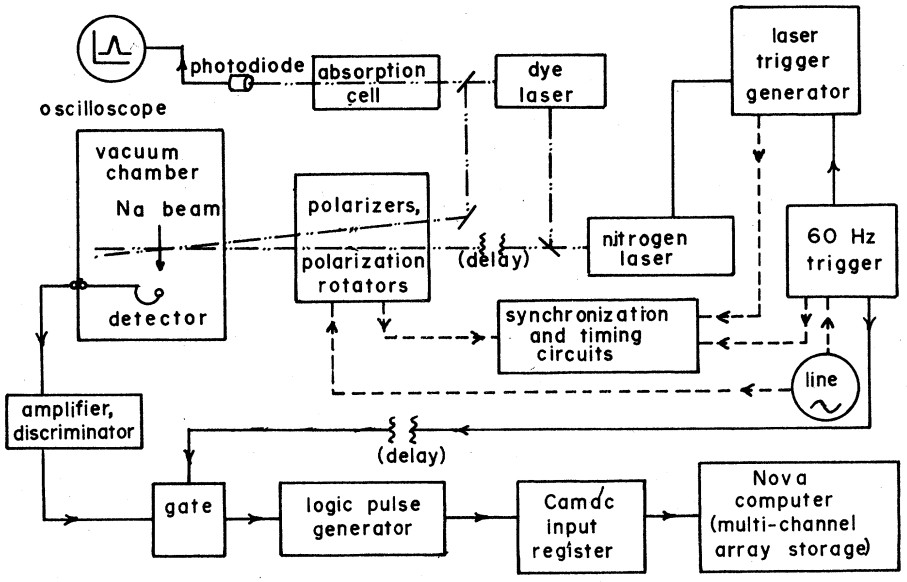

FIG. 3. Schematic diagram of the apparatus used in this experiment. The N_2L trigger was used only with the AVCO nitrogen laser. In the more recent experiments the signal gate was produced by the firing of the NRG laser rather than the 60-Hz trigger.

tuned to one or the other of the sodium *D* lines. Each laser beam passes through its own linear polarizer and moving polarization rotator. The laser beams range at an angle of approximately 2° in a vacuum chamber where they intersect a sodium beam at right angles. The photoelectrons are detected by a channel electron multiplier (Bendix Channeltron). Each electron pulse is converted into a digital logic pulse, gated, and stored in a Camac input register. The data is collected by a minicomputer (Nova 1220) and stored in a multichannel array.

The N_2L used in the first experiments performed on sodium[4,16] was an early AVCO model having a peak power of 25 kW at best. It produced a pulse at 3371 Å (3.68 eV) with duration 10 nsec full width at half-maximum (FWHM). Later experiments were done with an NRG nitrogen laser producing pulses 7–8 nsec long (FWHM) with a peak power of 400 kW.

The dye laser pumped by the N_2L is of the simple Hänsch design[17] with a folded delay path for a portion of the pumping N_2L beam.[18] A 3×10^{-3} *M* solution of rhodamine 6G in ethanol is used as the dye solution. It is stored in a 3-liter reservoir and pumped through a flowing dye cell. The beam initially emerging from the dye cell passes into a 20 × beam-expanding telescope 20 cm away from the dye cell and is reflected back by an 1800 lines/mm rotatable diffraction grating used in first order. At the other end of the cavity the DL light is focused by a quartz plano-convex lens whose plane side serves as a 4% reflecting output mirror. Between the output mirror and the dye cell is a parallel plate polarizer made of six equally spaced microscope slides mounted at Brewster's angle, which attenuates the unwanted polarization component. The total length of the DL cavity is 52 cm. The dye laser produces 4-nsec FWHM pulses with a conversion efficiency of 5%. At the sodium *D* line wavelengths it has a bandwidth of 0.25-Å FWHM.

A simple sodium absorption cell at 200–250 °C is used to tune the DL before each experiment is performed. The intensity of DL pulses passing through the absorption cell is measured with a PIN photodiode.

For the 3371-Å beam the polarizer is a calcite prism and the half-wave device is a quartz half-wave plate cut specifically for 3371 Å. For the visible beam the corresponding devices are a Wollaston prism and a quartz Fresnel rhomb, respectively.[19] Each half-wave device is in a rotating mount driven by motors synchronized to line frequency; the half-wave devices rotate at 1.5 Hz so that the axis of polarization of the linearly polarized light rotates at 3 Hz. Thus, with a fixed detector, the angular distribution over 180° can be sampled 6 times per second. This eliminates the effects of slow fluctuations in sodium beam intensity.

The interaction of the N_2L beam alone with the sodium beam is a significant source of background electrons. This problem is discussed in more detail below. In order to monitor these background electrons during an experiment, a chopper is placed in the DL beam path. It is attached to the N_2L polarization rotator and rotates at the same rate as the half-wave devices. Its effect is to allow 10 DL pulses to pass and to block the next 10

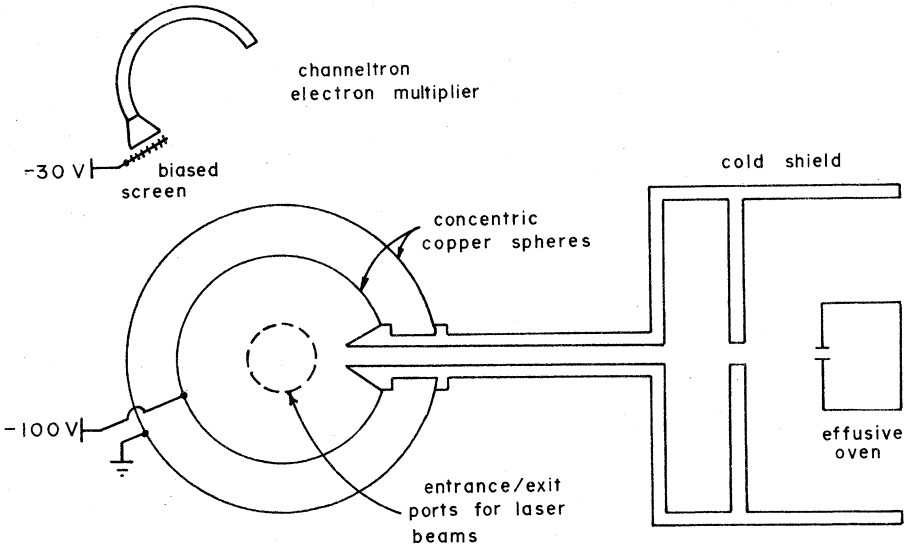

FIG. 4. Schematic diagram of the interior of the vacuum chamber. Na beams and electron trajectories are in the plane of the figure. Laser beams enter perpendicularly.

for a measurement of background alone. When the total signal and the background alone are alternately sampled several thousand times, a very accurate measurement of the background present in the total signal is obtained. When an experiment is completed, the signal channels are corrected for background to determine the net angular distribution.

The interior arrangement of the vacuum chamber is shown in Fig. 4. The chamber is pumped by a 6-in. diffusion pump to a typical operating pressure of 10^{-6} Torr. The sodium beam is produced by a simple effusive oven with a $\frac{1}{16}$-in. nozzle aperture. It is heated to 300°C by Nichrome heating wire, sufficient to produce a pressure of 10^{-5} Torr of Na in the beam or 10^{11} atoms/cm^3. The oven is surrounded by a water-cooled shield and the atomic beam is collimated by a tube, $\frac{1}{4}$ inch inside diameter, at the end of which are supported two concentric copper spheres whose centers are in the interaction region. The two laser beams enter through holes in these spheres along an axis perpendicular to the sodium beam. The inner sphere stands at a potential of −100 V, the outer sphere is grounded. Photoelectrons produced in the interaction region travel at their initial velocities to the inner sphere. Those in a plane perpendicular to the laser-beam axis pass through a high-transparency wire mesh grid, are accelerated, pass through a similar grid in the outer sphere, and are detected by the electron multiplier. In front of the multiplier is a small screen biased at −30 V to eliminate slow stray electrons. To preserve the linear trajectory of the 0.64-eV electrons the entire apparatus is surrounded by Helmholtz coils that reduce the magnetic field of the earth in the interaction region to less than 5 mG. The heating current of the oven is half-wave rectified and the laser is timed to fire only when the oven current is off.

The intensities of the laser beams and the sodium beam must be adjusted to given an appropriate counting rate of photoelectrons, neither so high that that counting system saturates nor so low that the signal and noise levels require long counting intervals. Saturation is a limitation because the electron multiplier and its associated circuitry are capable of detecting only one electron per laser pulse. Thus the counting system essentially saturates at 60 counts/sec and above 10 counts/sec we observe deviations from linearity. Hence the counting rate of signal electrons must be kept below 10 counts/sec. Also, the laser beam intensities must be low enough such that signal remains a linear function of both lasers; this assures that only the two-photon process is being observed and that no higher-order processes are involved.

There are two principal sources of background. The first is rf noise generated by the firing of the N_2L. Because the amplified electron signal occurs 0.4 μsec after the laser fires, it is possible to gate the detection circuitry so that spurious pulses produced by the rf noise are removed from the signal. Further reduction is obtained by intensity discrimination of the amplified electron pulses and by shielding of the N_2L. The rf noise is estimated to contribute less than 10% to the total background. The second kind of background consists of electrons produced when only the N_2L and the sodium beam are on. It is characterized by an isotropic angular distribution and an intensity proportional to the N_2L intensity and the sodium beam intensity. Surface photoionization is the presumed culprit. Apparently, the N_2L beam scat-

ters off free sodium in the beam and ionizes sodium atoms collected on the inner surface of the inner sphere. Since the sodium 4 ^2P transition at 3303 Å is close to 3371 Å, a strong Rayleigh scattering is implicated. We estimate that at least 100 photons are scattered per laser pulse. When no precautions are made to reduce it, the observed background rate can be as high as 100 counts/sec, high enough to make the signal unobservable. A technique that has reduced the background to workable levels is to oxidize the sodium on the surfaces. Oxidation of sodium in the gas phase is slow but proceeds quite rapidly on a surface. O_2 is bled into the chamber via a controlled leak so that the pressure is 5×10^{-5} Torr during an experiment. This method has reduced the N_2L background by a factor of 100.

With the more powerful NRG nitrogen laser neutral density filters are needed in both laser beams to bring the rate of photoionization into the linear region. With adequate laser beam attentuation the electron signal is linear in both laser intensities over more than two orders of their magnitudes. Typically, the N_2L pulse has a total energy of 2 μJ and the DL pulse has a total energy of 1.5 μJ in the interaction region. These values correspond to 3×10^{12} and 4×10^{12} photons, respectively. Under these conditions the signal counting rate is approximately 5 counts/sec and the background rate is approximately 1 count/sec.

Proper alignment of the laser beams is critical. Since the beams usually require daily alignment, a method was devised to do this without having to open the vacuum chamber. First, the N_2L beam is aligned along an axis known to pass through the center of the vacuum chamber where it intersects the sodium beam at right angles. Both laser beams are then reflected by a mirror in front of the chamber onto a target at the same distance in front of the mirror as the interaction region is behind it. Then the DL beam is directed onto the center of the N_2L beam at this distance. The area of overlap is approximately 3 mm $\times$ 3 mm.

When an electron strikes the multiplier a voltage pulse 20 nsec in duration and -5 to -20 mV high is produced. This pulse is amplified by an Ortec time pickoff unit, gated as explained above, converted to a +5 V TTL logic pulse and fed into a counter for visual display and into a Camac input register for computer acquisition. The minicomputer then stores the count in the appropriate location in a multichannel array.

To know what angle to assign to each of the ten channels of a 180° sweep of the angular distribution, the polarization direction of each polarizer and half-wave device combination must be known at each time the laser fires. To enable the determination of these angles a slot was cut in the edge of a rotating disc mounted on each polarization rotator. Each disc is straddled with an integrated circuit unit containing a matched light emitting diode (LED) and phototransistor. When the slot passes through the LED beam a reference pulse is generated. The polarization direction of each beam is measured with the rotators at their reference positions. The angle between the detector axis and the horizontal is also determined. When the half-wave devices are rotating, a high-frequency clock measures both the interval between the two reference pulses and the interval between the N_2L polarization reference pulse and the first laser pulse that follows. The first measurement gives the value of η, the angle between the two polarization vectors, and the second gives the value of θ corresponding to one of the channels. Since the polarizations rotate synchronously, η is fixed for all channels in a particular experiment. The value of θ for each succeeding channel differs by 18° from the one preceding it. The reference pulse from the N_2L polarization rotator is also sent to the computer through the Camac input register so that the computer may evaluate θ for each channel as well as distinguish between signal and background channels. This method of angle calibration gives values of θ and η correct to within 5°. A closer determination of these angles is available from the angular distributions themselves. This more accurate determination is described in the data analysis section that follows.

The timing and synchronization of various events is critical. It is useful to consider the overall sequence of events on several time scales.

First, on the nanosecond time scale shown in Fig. 5, the important events are the arrivals of the N_2L and DL beams at the interaction region. The shapes of the N_2L and DL pulses and the delay between them were measured on an oscilloscope taking its signal from a PIN photodiode with a rise time of about 1 nsec. The delay between the pulses, Δt, is adjusted by changing the path length of the N_2L beam.

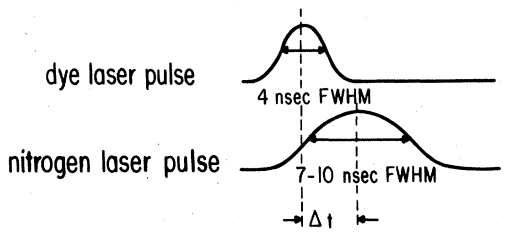

FIG. 5. Timing diagram for the nsec time scale. The width of the N_2L pulse depended upon which N_2 laser was used (see text). Experiments were performed at various values of Δt.

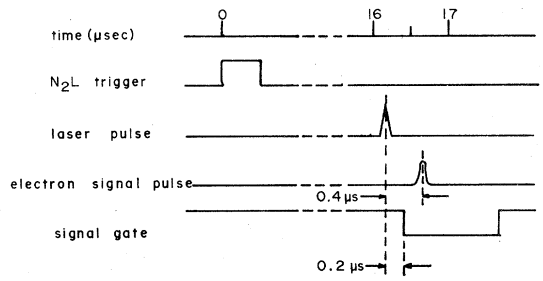

FIG. 6. Timing diagram for the μsec time scale. Shown here is the signal gate which separates the rf noise associated with the N_2 laser from the photoelectron signal.

On the μsec time scale shown in Fig. 6 the important consideration is the separation of the signal pulse produced by the electron multiplier from the rf noise of the nitrogen laser. This separation is achieved with the signal gate described above. The signal gate must open within 0.4 μsec of the N_2L pulse. When the AVCO laser was used the signal gate was produced by the N_2L trigger pulse, which occurred a few μsec before the laser fired. With the NRG laser a small portion of the N_2L beam is diverted into a photodiode to generate the signal gate. This method is necessary because this laser operates without a triggered spark gap and the time of firing has too much jitter (approximately 100 μsec) to enable the gate to be generated by an event preceding the actual laser pulse.

The sequences of events on the millisecond and second time scales are shown in Figs. 7 and 8. Before each experiment the half-wave rectified over-heating current, the timing of the laser pulses, and the phase of the DL beam chopper must be synchronized. The first constraint is that the laser must fire during the off phase of the heating current cycle and the second constraint is that ten laser pulses must be fired while the DL beam chopper is open, in such a way that they are unobstructed by the chopper. Since the DL beam chopper is driven by the same motor which rotates the N_2L half-wave plate, its reference pulse also indicates the angular location of the chopper slots. The second constraint leads to the requirement that a laser pulse occur during a 3-msec "window" after the N_2L polarization reference pulse, if every pulse in the 10-pulse train is to pass unobscured through the chopper.

The timing procedure was somewhat different for the two N_2 lasers. Because the phase of the heating current is difficult to adjust it is convenient to leave it fixed and synchronize the other events with respect to it. With the triggered AVCO laser its timing with respect to the line voltage was continuously adjustable. The most convenient timing method was to turn the N_2L polarization rotator on and off until the 3 msec chopper window happened to lie within the off cycle of the oven current. Then the N_2L trigger was adjusted to lie in the center of this window. The NRG laser, as mentioned, fires at a time fixed by the phase of the 60-Hz line current supplied to it. The first constraint is, therefore, automatically satisfied if the proper pair of phases from a 220 V three-phase line is used for the nitrogen laser. The timing of the chopper window must then be ad-

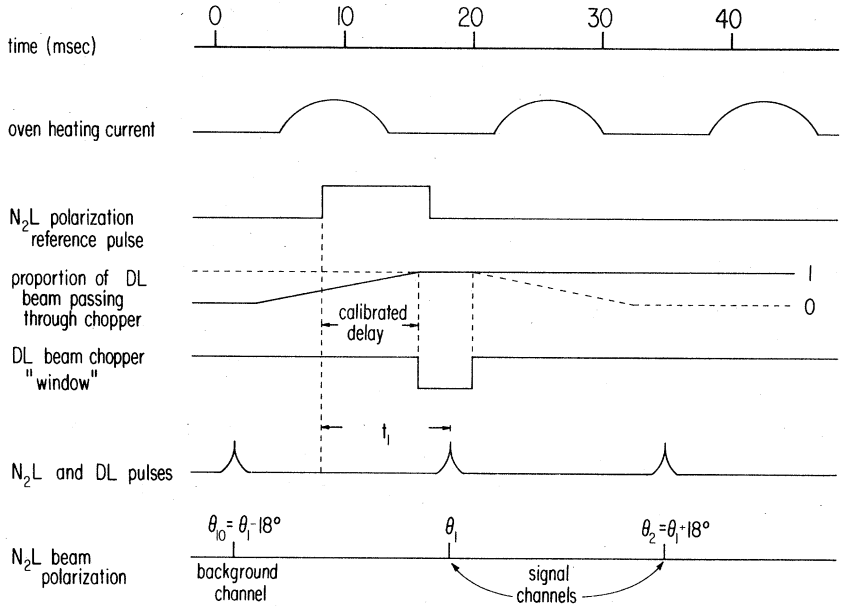

FIG. 7. Timing diagram for the msec time scale. The solid curve on the fourth line shows the proportion of DL beam passing through the chopper as it opens. The dashed curve shows the same quantity 9/60 second later as the chopper is closing. In order that neither the first DL pulse nor the tenth is partially obstructed by the chopper, the lasers must fire during the 3-msec window shown on the next line.

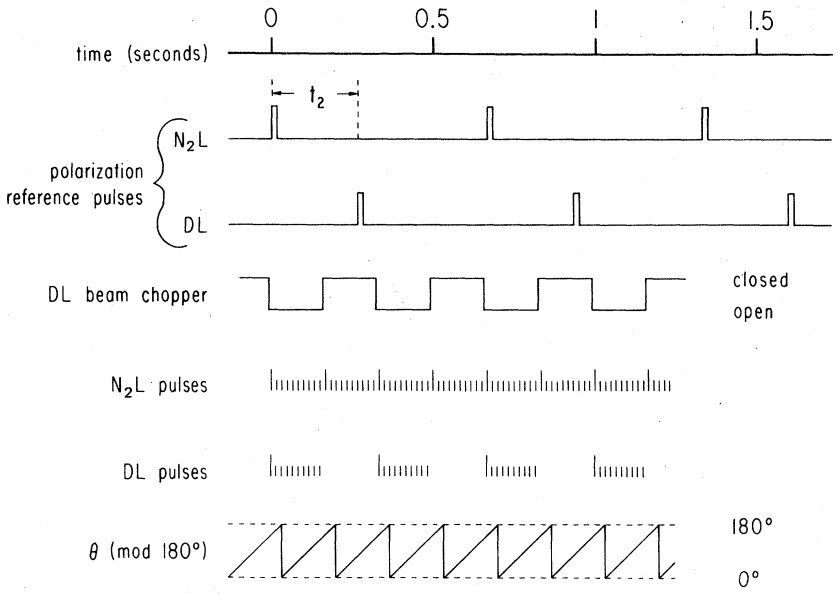

FIG. 8. Timing diagram for the seconds time scale. The total signal and the background alone are alternately sampled as the DL beam chopper opens and closes. The angular distribution is sampled at ten equally spaced angles from $\theta = 0°$ to 180°. A measurement of t_2 determines η, the angle between polarization vectors.

justed relative to the fixed laser pulse. This is done by making the phase of the line current to the N_2L polarization rotator continuously adjustable.

The measurement of a single angular distribution takes from 2 to 4 h depending on the signal and background counting rates. The data from a single experiment consists of a measurement of η, electron counts corrected for background in ten angular channels, and an absolute measurement of $\theta(\pm 5°)$ in one of the channels. The data collected by the minicomputer is stored for subsequent computer analysis.

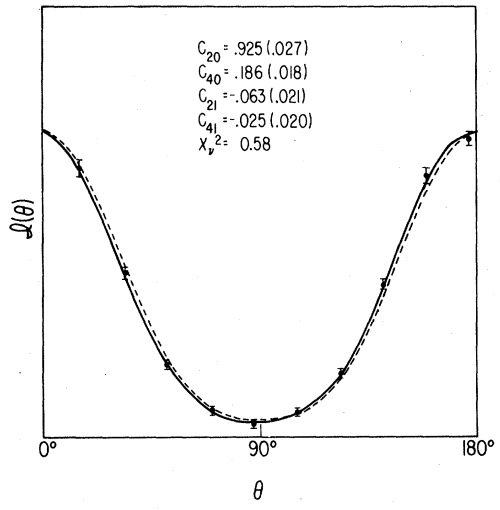

FIG. 9. Angular distributions of photoelectrons for $\eta = 0°$ and $\Delta t = 0$. The solid curves show least-squares fits of the measured angular distribution to Eq. (2), normalized to $c_{00} = 1$. The figure also gives the parameters of the fit, c_{LM}, with their standard deviations and the statistic χ_ν^2 (reduced chi squared). Data points and their uncertainties, reduced to the scale of the graphs, are shown here and in Figs. 13, 16, and 17. The dashed curves are the angular distributions expected from the best-fit values of the microscopic parameters.

DATA ANALYSIS

The goals of this analysis were to extract values of the atomic parameters σ_0/σ_2 and $\cos(\delta_0 - \delta_2)$, using the theoretical expressions (3), and to observe the effect of the hyperfine interaction on the angular distributions. Naturally, we wished to

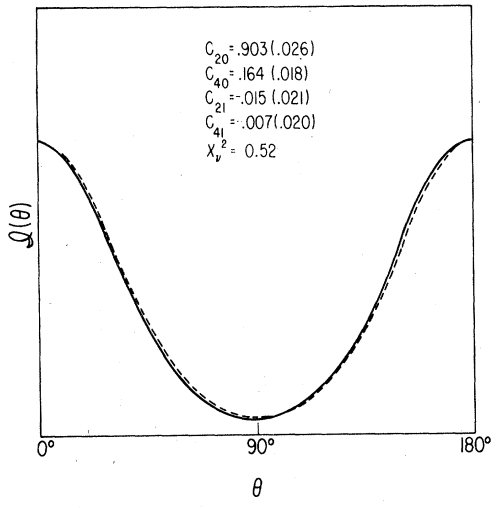

FIG. 10. Results for $\eta = 0°$, $\Delta t = 4$ nsec (see Fig. 9).

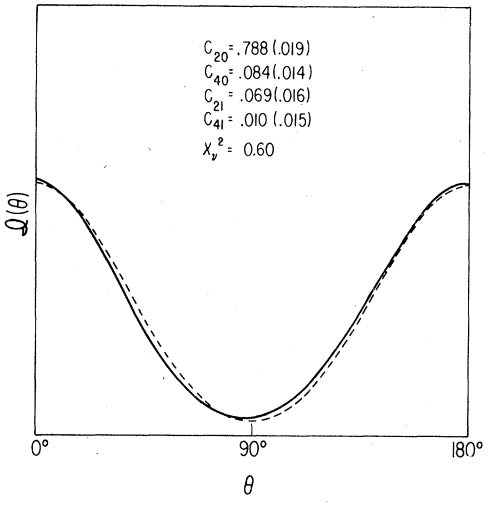

FIG. 11. Results for $\eta = 0°$, $\Delta t = 6.5$ nsec (see Fig. 9).

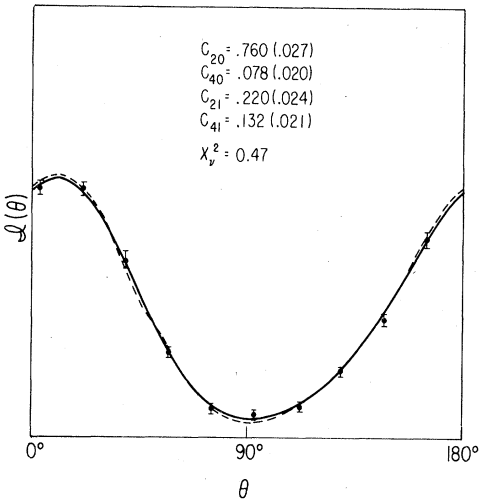

FIG. 13. Results for $\eta = 28°$, $\Delta t = 4$ nsec (see Fig. 9).

compare the results with theoretical predictions.

Each angular distribution, measured as described above, was corrected for background and fit by a least-squares method to the phenomenological equation (2). Since the total cross section is not measured, the relevant quantities are not the coefficients C_{LM}, but rather their ratios. To place different angular distributions on a common basis the coefficients reported here are normalized to $C_{00} = 1$. Some examples of our measurements are shown in Figs. 9–17. Other angular distributions entering into this analysis are reported elsewhere.[4,5] Experimental points are shown on a few of the figures; the error bars are typical for all the results. The reduced chi-squared values are given for all curves.

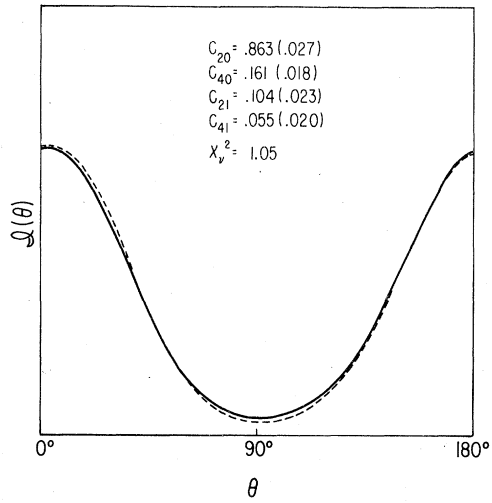

FIG. 12. Results for $\eta = 12°$, $\Delta t = 4$ nsec (see Fig. 9).

We first observe that qualitatively they have the forms suggested by Eqs. (2) and (3). As η is increased from 0° to 90°, the P_{40} term decreases and changes sign, as expected from Eq. (3), being negative for $\eta = 90°$. Also, the angular distributions at $\eta = 0°$ and 90° satisfy the condition that they are symmetric about $\theta = 90°$. At other η they are not symmetric with respect to $\theta = 90°$, as evidenced by the appearance of the antisymmetric terms P_{21} and P_{41}. We further observe, from the $\eta = 0$ angular distributions in Figs. 9–11, that the P_{40} term becomes less important for greater time delays,

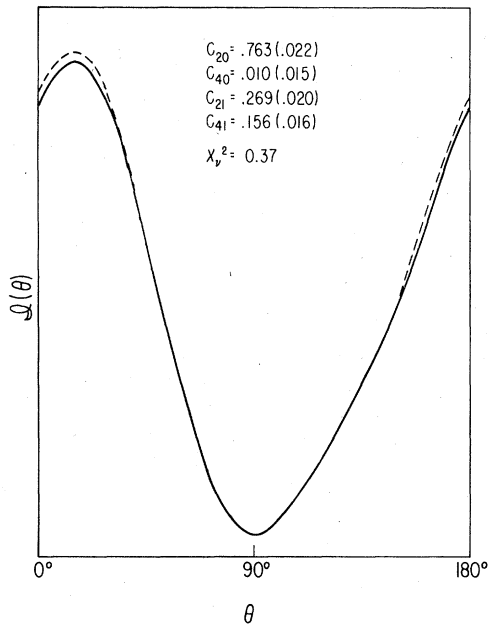

FIG. 14. Results for $\eta = 44°$, $\Delta t = 4$ nsec (see Fig. 9).

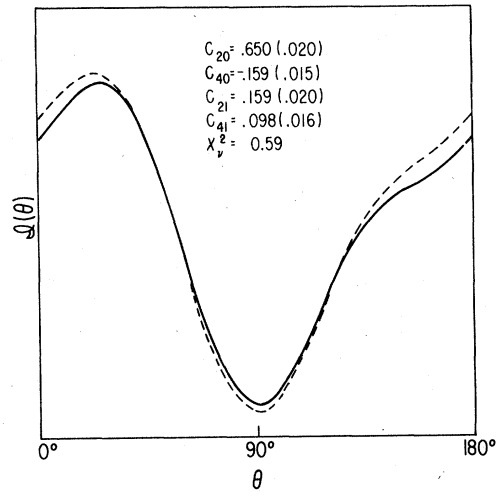

FIG. 15. Results for $\eta = 74°$, $\Delta t = 4$ nsec (see Fig. 9).

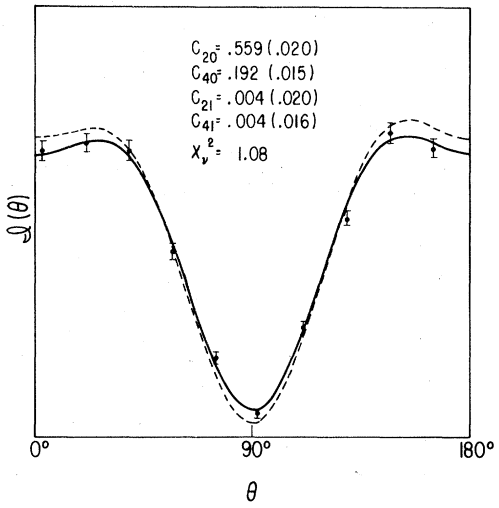

FIG. 17. Results for $\eta = 91°$, $\Delta t = 4$ nsec (see Fig. 9).

consistent with the predictions of the theory regarding the hyperfine interaction in the intermediate state. This was also seen to be true for angular distributions with $\eta = 90°$.[5]

The fact that there are symmetry restrictions at $\eta = 0°$ and 90° gives a good method of calibrating both θ and η. Measurements near $\eta = 90°$ proved to be most useful for this purpose. It happens that these angular distributions have two maxima, whose relative magnitudes are very sensitive to the precise value of η. At $\eta = 90°$ these two maxima must have equal intensity and the angular distributions must be symmetric about $\theta = 90°$. With several measurements near this value of η, θ and η were recalibrated so that these two conditions were met. We estimate the standard deviation in the recalibrated values to be about 1°.

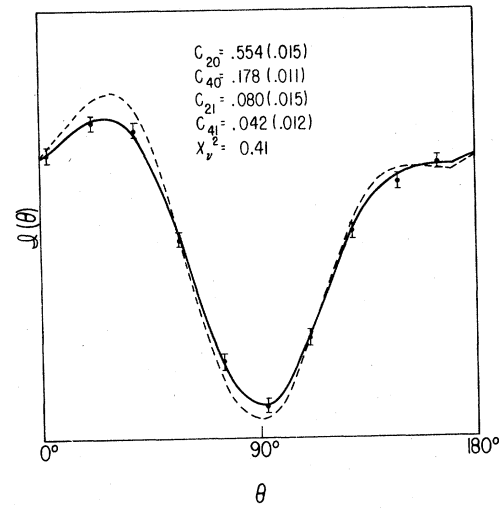

FIG. 16. Results for $\eta = 82°$, $\Delta t = 4$ nsec (see Fig. 9).

Because of the sensitivity of the results to the precise characteristics of the laser pulses, it was deemed desirable to determine the atomic parameters from quantities independent of $\chi(2)/\chi(0)$. It is possible to do even better because one can use quantities which are independent of η as well. From Eqs. 3 we find

$$\tfrac{3}{2}\sqrt{5}\,C_{20} + \tfrac{15}{8}\,C_{40} = \tfrac{1}{9}[2\chi(0) + (2 - 3\sin^2\eta)\chi(2)] \times [-2\sigma_0\sigma_2\cos(\delta_0 - \delta_2) + \sigma_2^2]$$

and

$$C_{00} + \sqrt{5}\,C_{20} + 3C_{40} = \tfrac{1}{27}[2\chi(0) + (2 - 3\sin^2\eta)\chi(2)] \times [\sigma_0^2 - 4\sigma_0\sigma_2\cos(\delta_0 - \delta_2) + 4\sigma_2^2].$$

The ratio $\mathcal{R}$ of these two quantities is independent of $\chi(0)$, $\chi(2)$, and η. This ratio was computed for each measured angular distribution from its least-squares fit. Its value was observed to be independent of both η and Δt to within the estimated experimental uncertainties. The best value from our data is

$$\mathcal{R} = \frac{-6(\sigma_0/\sigma_2)\cos(\delta_0 - \delta_2) + 3}{(\sigma_0/\sigma_2)^2 - 4(\sigma_0/\sigma_2)\cos(\delta_0 - \delta_2) + 4} = 0.95 \pm 0.02\,. \tag{4}$$

This quantity is directly related to the ratio $I(0°)/I(90°)$ of the intensities at $\theta = 0°$ and $\theta = 90°$, which is also expected to be independent of η and $\chi(2)/\chi(0)$. The reason $I(0°)/I(90°)$ is independent of η and $\chi(2)/\chi(0)$ is that only the $3p$ atomic orbital with $m_l = 0$ in the intermediate state contributes to the photoelectron intensity at these two angles.

For the same reason, $I(0°)/I(90°)$ and the ratio $\chi(2)/\chi(0)$ should be the same for both members of the doublet ($j=\frac{1}{2}$ or $j=\frac{3}{2}$) of the ^1P state excited in the first transition, provided that the $3s \rightarrow 3p$ radial matrix elements and the parameters σ_0/σ_2 and $\cos(\delta_0-\delta_2)$ are the same for these two intermediate states.

The photoelectron distribution from the $3p\,^2P_{1/2}$ state was measured by Duncanson *et al.*[4] and fit by least squares to $a_0+a_1\cos^2\theta$.[4] The quantity defined by Eqs. (4) is theoretically equivalent to the coefficient a_1 from this fit. The least-squares value of $a_1(0.959)$ entered into the determination of the best value of the parameter in Eq. (4).

Beyond this we need one more relation between σ_0/σ_2 and $\cos(\delta_0-\delta_2)$. Such a relation exists whenever $\eta \neq 0°$ or 90° and the angular distributions contain the antisymmetric terms P_{21} and P_{41}. The relation is

$$-(\sigma_0/\sigma_2)\cos(\delta_0-\delta_2)=\tfrac{4}{7}\sqrt{\tfrac{3}{2}}\,C_{21}/C_{41}-\tfrac{2}{7}$$

and we see that it too is independent of η and $\chi(2)/\chi(0)$. The best value from our data is

$$(\sigma_0/\sigma_2)\cos(\delta_0-\delta_2)=-0.89\pm0.08\,. \tag{5}$$

Combining the relations (4) and (5), we find $\sigma_0/\sigma_2=-1.11$ (standard deviation $=0.10$) and $\cos(\delta_0-\delta_2)=0.81$ (standard deviation $=0.09$).

Since theoretical calculations have given σ_0 as a negative number and σ_2 as a positive number, we have made the choice that σ_0/σ_2 is negative. Changing the signs of both σ_0/σ_2 and $\cos(\delta_0-\delta_2)$, however, gives values equally consistent with our data.

The least-squares coefficients also provide us with a check on the angle calibration at all η. From Eq. (3) we find

$$\tan 2\eta = 2C_{41}/\sqrt{5}\,C_{40}\,. \tag{6}$$

Thus, from a least-squares fit, we can calculate the value of η. This is a useful test of the calibration of θ as well as η because coefficients determined by least squares are sensitive to errors in θ. From Eq. (6) η was calculated for each least-squares fit. In no case did the calculated value differ from the presumed value by more than 3°.

Finally, we compute the quantity $\chi(2)/\chi(0)$ from the empirical coefficients and the newly derived atomic parameters. Dividing the expression for C_{00} by that for C_{40} in Eq. 3, we obtain a relation among $\chi(2)/\chi(0)$, σ_0/σ_2, $\cos(\delta_0-\delta_2)$, and η:

$$\frac{C_{00}\chi(2)}{C_{40}\chi(0)}\cos 2\eta=\tfrac{280}{9}\left[\left(\frac{2+(2-3\sin^2\eta)\chi(2)}{\chi(0)}\right)\times\frac{\sigma_0}{\sigma_2}+\left(\frac{4+(\frac{6}{5}\sin^2\eta+\frac{2}{5})\chi(2)}{\chi(0)}\right)\right]. \tag{7}$$

Thus, if η and the atomic parameters are known, we can solve for $\chi(2)/\chi(0)$ from each angular distribution. For the different time delays the best values are

$$\chi(2)/\chi(0)=0.73\pm0.10 \quad \text{at } \Delta t=0$$
$$=0.635\pm0.050 \quad \text{at } \Delta t=4 \text{ nsec}$$
$$=0.38\pm0.10 \quad \text{at } \Delta t=6.5 \text{ nsec}\,.$$

The above values are for measurements made using the NRG nitrogen laser. A set of measurements made with the AVCO nitrogen laser[4] at a Δt of 5 nsec gave 0.71 ± 0.10 as the best value of $\chi(2)/\chi(0)$. These values are all somewhat larger than expected from the theoretical analysis based on Gaussian pulse shapes.[5] One explanation could be deviation from Gaussian shapes. Alternatively, the large ratio of $\chi(2)/\chi(0)$ might be due to depletion of the intermediate state by the second laser pulse. This nonlinear effect is not included in the theoretical analysis and would tend to decrease the intermediate state population seen by the later part of the ionizing pulse, thus decreasing the importance of longer time delays. Since $\chi(2)/\chi(0)$ decreases with increasing Δt, for Δt <10 nsec the net effect would be higher measured values of $\chi(2)/\chi(0)$. However, based on a measured 2 μJ per pulse and a cross section for ionization of 5×10^{-16} cm^2 (see below), we estimate there would be a depletion of only 0.1%, probably too low to account for the ratio $\chi(2)/\chi(0)$. Hence we are inclined to attribute the discrepancy to the pulse shapes.

DISCUSSION

Above threshold, one expects the phase shift δ_l to be given by

$$\delta_l=\arg\Gamma(l+1-i/k)+\pi\mu_l(\epsilon)\,, \tag{8}$$

where k is the electron's momentum in atomic units and $\mu_l(\epsilon)$ is the extrapolated quantum defect. From bound-state data,[20,21] we expect

$$\mu_0(\epsilon)=1.345, \quad \mu_2(\epsilon)=0.0169$$

at $\epsilon=0.64$ eV, leading to

$$\cos(\delta_0-\delta_2)=0.92\,.$$

Theoretical predictions of μ_0 and μ_2 at threshold indicate a value of $\cos(\delta_0-\delta_2)$ between 0.88 and 0.92.[22] These results are not greatly different than our experimental value of 0.81 ± 0.09.

There is, however, some discrepancy in the ratio σ_0/σ_2. The calculations of Burgess and Seaton[23] and of Rudkjöbing[24] indicate a value between -0.64 and -0.72. From the more recent calculations of Laughlin[25] we infer a value of -0.68 as

compared to our measured value of -1.11 ± 0.10. The total photoionization cross-section measurements of Rothe[26] also show some disagreement with these calculations; the measured total cross section is somewhat higher than expected from theory, except for energies very near threshold. Furthermore, Laughlin[25] suggests that Rothe's results should be raised further by 10% because of his use of an inaccurate gf value. Using the corrected experimental cross section and our value of σ_0/σ_2 one may determine the partial photoionization cross sections Q_0 and Q_2 for production of s and electrons. The cross sections are related to the radial matrix elements by

$$Q_0/Q_2 = \tfrac{1}{2}(\sigma_0/\sigma_2)^2 . \quad (9)$$

At 0.64 eV we find values of 1.8×10^{-18} and 2.95×10^{-18} cm^2, respectively. Laughlin's calculations give partial cross sections of 0.7×10^{-18} cm^2 for s electrons and 3.05×10^{-18} cm^2 for d electrons at this energy. Thus these experiments seem to indicate that previous calculations of the s-wave radial matrix element are low by a factor of about 40% at this energy, while calculations of the d-wave radial matrix element are substantially correct.

ACKNOWLEDGMENTS

This research was supported by a grant from the National Science Foundation. The authors would like to thank W. C. Lineberger for suggesting the introduction of traces of oxygen to reduce the electron background.

*Present address: Dept. of Chemistry, Iowa State Univ., Ames, Iowa 50011.

[1]J. C. Tully, R. S. Berry, and B. J. Dalton, Phys. Rev. 176, 95 (1968).
[2]M. Lambropoulos and R. S. Berry, Phys. Rev. A 9, 1992 (1974).
[3]S. Edelstein, M. Lambropoulos, J. Duncanson, and R. S. Berry, Phys. Rev. A 9, 2459 (1974).
[4]J. A. Duncanson, Jr., M. Strand, A. Lindgård, and R. S. Berry, Phys. Rev. Lett. 37, 987 (1976).
[5]M. Strand, J. Hansen, R. L. Chien, and R. S. Berry, Chem. Phys. Lett. 59, 205 (1978).
[6]C. N. Yang, Phys. Rev. 74, 764 (1948).
[7]W. Zernik, Phys. Rev. 135, A51 (1964).
[8]E. Arnous, S. Klarsfeld, and S. Wane, Phys. Rev. A 7, 1559 (1973).
[9]R. A. Fox, R. M. Kogan, and E. J. Robinson, Phys. Rev. Lett. 26, 1416 (1971).
[10]J. Copper and R. Zare, J. Chem. Phys. 48, 942 (1968).
[11]A. Buckingham, B. Orr, and J. Sichel, Philos. Trans. R. Soc. London A 268, 147 (1950).
[12]U. Fano and D. Dill, Phys. Rev. A 6, 185 (1972).
[13]E. H. A. Granneman, M. Klewer, K. J. Nygaard, and M. J. van der Wiel, J. Phys. B 9, 865 (1976).
[14]E. H. A. Granneman, M. Klewer, G. Nienhuis, and M. J. van der Wiel, J. Phys. B 10, 1625 (1977); G. Nienhuis, E. H. A. Granneman, and M. J. van der Wiel, *ibid.* 11, 1203 (1978).
[15]M. P. Strand, Ph.D. thesis, University of Chicago, 1979 (unpublished); M. P. Strand and R. S. Berry (unpublished).
[16]J. A. Duncanson, Ph.D. thesis, University of Chicago, 1976 (unpublished).
[17]T. W. Hänsch, Appl. Opt. 11, 895 (1972).
[18]J. E. Lawlor, W. A. Fitzsimmons, and L. W. Anderson, Appl. Opt. 15, 1083 (1976).
[19]R. W. Anderson, Appl. Opt. 13, 1100 (1974).
[20]P.d.P. Risberg, Ark. Fys. 10, 583 (1956).
[21]T. F. Gallagher, R. M. Hill, and S. A. Edelstein, Phys. Rev. A 13, 1448 (1976).
[22]C. Jaffe and W. P. Reinhardt, J. Chem. Phys. 66, 1285 (1977).
[23]A. Burgess and M. J. Seaton, Mon. Not. R. Astron. Soc. 120, 121 (1960).
[24]M. Rudkjöbing, Publ. Københavens Obs. 18, 1 (1940).
[25]C. Laughlin, J. Phys. B 11, 1399 (1978).
[26]D. E. Rothe, J. Quant. Spectrosc. Radiat. Transfer 9, 49 (1969).